bioRxiv preprint doi: https://doi.org/10.1101/375923; this version posted July 24, 2018. The copyright holder for this preprint (which was not certified by peer review) is the author/funder. All rights reserved. No reuse allowed without permission.

A new actin depolymerase: a catch bond Myosin 1 motor

Short title: *A catch-bond Myosin depolymerizes actin*

Julien Pernier[1,2,3]*, Remy Kusters[1,2]*, Hugo Bousquet[2,3], Thibaut Lagny[1,2,3], Antoine Morchain[1,2], Jean-François Joanny[1,2,4], Patricia Bassereau[1,2]+, Evelyne Coudrier[2,3]+

1. Laboratoire Physico Chimie Curie, Institut Curie, PSL Research University, CNRS UMR168, 75005 Paris, France
2. Sorbonne Universités, UPMC University Paris 06, 75005 Paris, France
3. Institut Curie, PSL Research University and C.N.R.S. UMR 144, 26 rue d'Ulm, Paris, France
4. ESPCI Paris, PSL Research University, 10 rue Vauquelin 75005 Paris, France

* : equally contributing authors
+ corresponding authors: patricia.bassereau@curie.fr and evelyne.coudrier@curie.fr

Sentence summary

Due to its catch bond, Myosin 1b depolymerizes sliding actin filaments at their barbed end by exerting a prolonged force.

bioRxiv preprint doi: https://doi.org/10.1101/375923; this version posted July 24, 2018. The copyright holder for this preprint (which was not certified by peer review) is the author/funder. All rights reserved. No reuse allowed without permission.

Abstract

The regulation of actin dynamics is essential for various cellular processes. Former evidence suggests a correlation between the function of non-conventional myosin motors and actin dynamics. We investigate the contribution of the catch-bond Myosin1b to actin dynamics using sliding motility assays. We observe that sliding on Myosin1b immobilized or bound to a fluid bilayer enhances actin depolymerization at the barbed end, while sliding on the weak catch-bond MyosinII has no effect. Our theoretical model supports that the catch-bond prolongs the attachment time of the motor at the barbed end due to the friction force exerted by the sliding filament; thereby this motor exerts a sufficient force on this end to promote depolymerization. This work reveals a non-conventional myosin motor as a new type of depolymerase.

bioRxiv preprint doi: https://doi.org/10.1101/375923; this version posted July 24, 2018. The copyright holder for this preprint (which was not certified by peer review) is the author/funder. All rights reserved. No reuse allowed without permission.

Actin filaments (F-actin) form a variety of dynamical architectures that govern cell morphology and cell movements. The dynamics of the actin networks are regulated in space and time by the assembly and disassembly of actin polymers under the control of regulatory proteins. Cortical actin organizes lateral movement of transmembrane proteins and participates in membrane signaling by interacting transiently with the plasma membrane (*1*). One class of actin-associated molecular motors, the single-headed myosin 1 proteins, bridges cortical actin to the plasma membrane. Polymerization of actin filaments at the plasma membrane generates forces on the membrane as well as on their membrane linkers. Inversely myosin 1 can exert and sustain pN forces on F-actin (*2*).

This important class of myosins contains a motor domain at its N-terminus that binds F-actin in response to ATP hydrolysis, a light chain binding domain (LCBD) that binds calmodulin (in most cases), and a Tail domain at the C-terminus (Fig. 1A) (*3*). The Tail domain encompasses a tail homology domain (TH1) with a pleckstrin homology motif (PH) that binds phosphoinositides (Fig. 1A). Beside the involvement of myosin 1 proteins in a large variety of cellular processes including cell migration and membrane trafficking (*3*), manipulation of myosin 1 expression has revealed a correlation between these myosins and actin network architecture (*4-7*). In particular, down- or overexpression of one of these myosins, myosin 1b (Myo1b), affects the organization of the actin cytoskeleton in the juxtanuclear region of HeLa cells (*4*) and in growth cones of cortical neurons (*6*). However, a role of these motors in actin dynamics remains to be explored.

Given that Myo1b is mechanosensitive and is a catch bound motor (the time Myo1b remains bound to F-actin strongly increases with an applied load), Myo1b could in turn exert a force on polymerizing actin filaments (*8, 9*). When bound to a substrate and in contact with F-actin, Myo1b has different configurations over time as a function of the ATP hydrolysis stage. When is attached, it first performs its power-stroke and propels the actin filament over a distance *d* towards the minus-end (being a plus-end motor). Due to its catch-bond behavior, it then remains passively attached to the filament for a time that depends on the applied force F. It eventually detaches with a force-dependent detachment rate $\varpi_{det}(F)$ (Fig. 1B). Increasing the force on the filament hence decreases the detachment rate, which in turn could impact the growth of actin filaments. In this report, we use *in vitro* F-actin gliding assays (Fig. 1C) and total internal reflection fluorescence (TIRF) microscopy to study the effect of Myo1b on actin polymerization dynamics, with the motors either immobilized on a solid substrate (Fig. 1C, III) or bound to a fluid supported bilayer, which mimics cell membranes (Fig. 1C, IV).

The sliding velocity v_f of single stabilized F-actin on Myo1b immobilized on a glass coverslip (Fig. S1A, top and Movie S1) and the sliding velocity v_f and the polymerisation rate v_p of single polymerizing F-actin (Fig. S1A, bottom and Movie S2) (Supplementary Materials) were measured by image analysis. At high Myo1b density (8000 μm^{-2}) (for the motor density measurement, see Supplementary Materials and Fig. S1B), both stabilized and polymerizing filaments move with the same average sliding velocity $v_f = 56.4 \pm 15.4$ nm.s^{-1} and $v_f = 53.9 \pm 5.5$ nm.s^{-1}, respectively (Figure 2A, Movies S3, S4 and Table S1) in the presence of 2 mM ATP (above saturation for motor activity) (*10*) (Fig. 2A and Fig. 2B). In both cases, this velocity decreases by about a factor two when decreasing the Myo1b density by a factor of twenty (Fig. S2B, C, Table S1) or when reducing the ATP level to 0.2 mM (Fig. 2A,B, Movies S3, S4, S5) below saturation for Myo1b, but not affecting actin polymerization (Table S2).

In a two-state cross-bridge model (Fig. S3A) with explicit ATP dependence (*11*) (Supplementary Materials), lowering the ATP concentration decreases the fraction of attached motors that perform a power stroke, thus increasing the fraction of attached motors that do not

bioRxiv preprint doi: https://doi.org/10.1101/375923; this version posted July 24, 2018. The copyright holder for this preprint (which was not certified by peer review) is the author/funder. All rights reserved. No reuse allowed without permission.

contribute to filament propulsion. By calculating the stationary sliding velocity of the filament, our model does predict a decrease in sliding speed by lowering the ATP concentration (from $v_f \approx 55\,nm/s$ at a $C_{ATP} = 2mM$ to $v_f \approx 43.5\,nm/s$ at $C_{ATP} = 0.2mM$, see Fig. S3D, E). Likely due to the approximations made for the ATP-dependence of the kinetics (ω_{det}, ω_{on}) and for the mechanical parameters (k_c, b) of the motor (further discussed in the Supplementary Materials), the predicted decrease in filament sliding speed is smaller than that observed in the measurements (Fig. 2B and Table S1).

After confirmation that the filament sliding velocities are in good agreement with previous reports and that the model accounts well for our data, we investigated the impact of Myo1b on actin polymerization upon filament sliding. The actin assembly-disassembly kinetics are an order of magnitude faster at the barbed (plus) end than at the pointed (minus) end (*12*). Thus, we measured the elongation ΔL of F-actin at the barbed-end versus time (Fig. 2C). Strikingly, filament sliding on Myo1b decreases the actin polymerization rate v_p, as compared to actin polymerization in the absence of Myo1b (Fig. 2D and Movie S6). This effect is stronger for high filament sliding velocity (in the presence of 2 mM ATP) and reduced at lower Myo1b density on the substrate (Fig. S2B, Fig. S2D, Movie S5 and Table S2). We also measured the dynamics of the pointed (minus) end by detecting the relative movement of this extremity compared to a fiducial point on the filament. In contrast with the barbed end, we did not observe any filament length variation (Fig. S2A and Movie S7), thus filament sliding on the motors reduces the actin polymerization rate at the barbed-end only. As a control, we tested the impact on actin polymerization of free Myo1b present only in the bulk, or immobilized but inactivated (Fig. S2B,D and Movie S8); we did not observe any effect on polymerization (Fig. S2E). Moreover, although actin filaments slide five-fold faster on non- or weak catch-bond myosins such as muscle Myosin II (*13*), at the same bulk monomeric-actin (G-actin) concentration (Fig. 2A,B and Movie S9), the actin polymerization rate remains similar to the control (Fig. 2C, D). These observations demonstrate that an **immobilized myosin motor** with **intact activity** and a **catch-bond behavior** reduces actin polymerization rate at the barbed-end up to a factor two (Table S2), in contrast to a weak catch-bound myosin such as muscle Myosin II.

Dynamics at the barbed-end results from a balance between the rate of association of G-actin k_{on} and the rate of dissociation k_{off}; steady state is obtained at the critical concentration C_{c^+}. Classically, these dynamical parameters are deduced from the measurement of the variation of the polymerization rate v_p with G-actin concentration C_m: $v_p = k_{on}C_m - k_{off}$. By varying the G-actin bulk concentration from 0.1 to 1 µM in the presence of either 0.2 mM and 2 mM ATP, we observed that the slope corresponding to k_{on} is unchanged when F-actin slides over Myo1b, whereas C_{c^+} which is the ratio between k_{off} and k_{on} increases (Fig. 2D) demonstrating that k_{off} increases in these conditions (Fig. 2D and Table S2). At a G-actin concentration (0.3 µM) above the critical concentration (0.1 µM) of the barbed end in the absence of Myo1b, filaments sliding over Myo1b stop polymerizing (Fig. S2F, G and Movie S10). Interestingly, the dissociation rate is weakly affected when reducing Myo1b density (Fig. S2E and Table S2). The decrease of the dissociation rate is due to a lower sliding velocity of the filament. As expected, the sliding velocity of the filament decreases weakly with the motor density. In our model, this effect is associated with the impact of the external hydrodynamical friction on the filament, which eventually slows down the motors. In contrast, while sliding on Myosin II is much faster, this myosin has no influence on k_{off} at the barbed-end of the filament (Fig. 2D and Table S2). Together, these observations indicate that the catch-bond Myo1b is an actin depolymerase.

bioRxiv preprint doi: https://doi.org/10.1101/375923; this version posted July 24, 2018. The copyright holder for this preprint (which was not certified by peer review) is the author/funder. All rights reserved. No reuse allowed without permission.

One possible mechanism for this property is that Myo1b induces actin depolymerisation by modulating the torsion of the filaments *(14)*. In this case, polymerization kinetics would be expected to depend on the filament length with the twist gradient being inversely proportional to the length. However this is not what we observe (Fig. S2H), excluding an explicit role of filament torsion due to motor attachment along the filament.

We thus developed a theoretical model for actin polymerization when filaments slid on motors with catch-bond properties (Fig. 2E, Fig. S3, and Supplementary Materials). Since the motor detachment rate decreases with increasing filament sliding velocity due to the catch-bond behavior, the motors induce a larger friction force on the sliding filaments as compared to non-catch bond motors such as Myosin II. We hypothesize that this friction force generated along the filament increases the attachment time of the single molecular motor at the barbed end and thus this motor induces a force at this extremity sufficient to promote depolymerization. We have quantified this effect by assessing the force exerted on the last motor, taking into account a catch-bond like detachment rate within our two-state cross-bridge model (Supplementary Materials) *(15)*. The time-averaged friction force along the filament increases when increasing the ATP concentration. The friction forces are of the order of 0.1-1 pN (Supplementary Materials), in the range where they are expected to alter the monomer association-dissociation kinetics *(16)*.

In our model the actin dissociation rate increases exponentially with the applied force. The characteristic force of this exponential increase is found to be $F^* \approx$ 6-10 pN. A characteristic force of 10 pN or larger would make the actin filament insensitive to forces applied by the motor (Fig. S4A). A too small force would impact the dissociation at low ATP concentration, precluding the stability of the filaments in the presence of motors (Fig. S4A). This model relates Myo1b catch-bond behavior and our observations that F-actin depolymerization at the barbed-end is accelerated when filaments slide on top of these motors.

In cells, Myo1b is bound to the fluid plasma membrane lipid bilayer through the interaction of its PH domain with PI(4,5)P2 *(17)*, and thus it is not immobilized (Fig. 3A). We mimic experimentally these cellular conditions by analyzing the impact of Myo1b on actin dynamics when bound to a glass-supported lipid bilayer (SLB) composed of 79.5% POPC, 20% L-α-phosphatidylinositol-4,5-bisphosphate (PI(4,5)P2) and 0.5% Rhodamine-PE or Atto488-DOPE (mol/mol) (Fig. 1C, II and IV) (Supplementary Materials). We checked using fluorescence recovery after photobleaching (FRAP) that membrane fluidity was preserved in the SLB with bound Myo1b (Fig. 3A). The lipid diffusion coefficient was in agreement with data published on SLBs composed of pure POPC *(18)*. After recruitment on the SLB, Myo1b diffuses freely in the plane of the membrane (Fig. 3A). In addition, the lipids continue to diffuse freely even when Myo1b diffusion is strongly decreased by a dense actin network (Fig. 3A) due to an emerging coupling when a filament bridges multiples motors. The diffusion coefficients are close to those measured in cell membranes (Fig. 3A), showing that in our *in vitro* experiments, the fluidity of the membrane is preserved. As previously reported *(19)*, myosin 1 proteins bound to a lipid bilayer exert a force strong enough to propel actin filaments in spite of the fluidity of the support. We confirmed that in the presence of 2 mM ATP and at a similar Myo1b density as when immobilized (8500 μm^{-2}), stabilized and polymerizing F-actin slides on Myo1b bound to SLBs, although with a velocity reduced by about 25%: v_f = 37.6 ± 7.3nm.s^{-1} and v_f = 39.3 ± 8.2nm.s^{-1} respectively (Fig. 3B, Fig. 3C, Movie S11 and Table S1).

We have calculated the relative contributions of the viscous drag of the bulk and of the lipid bilayer on the motion of the filaments. First, we have considered F-actin moving in water ($\eta_b = 10^{-3} Pa.s$) above Myo1b bound to a SLB (Fig. 3D). We estimate that, since the

bioRxiv preprint doi: https://doi.org/10.1101/375923; this version posted July 24, 2018. The copyright holder for this preprint (which was not certified by peer review) is the author/funder. All rights reserved. No reuse allowed without permission.

in-plane viscous drag between the motor and the lipid bilayer is much larger than the bulk viscosity experienced by the actin filaments, the velocity of the filament-motor couple, v_m, practically vanishes. Thus, filaments slide with a velocity $\tilde{v}_f$ similar to that measured for immobilized motors: $\tilde{v}_f \approx v_f$ (Fig. S4B). However, the presence of methyl-cellulose in the assay to maintain the F-actin in the vicinity of the bilayer and crowding effects between nearby filaments significantly increases the effective viscosity of the bulk. This reduces the effective sliding speed of the filament $\tilde{v}_f$ since part of the sliding is dissipated by in-plane motion of the motors in the bilayer (Fig. S4B). This can explain why in our experiments, F-actin moves over SLB-bound Myo1b but with a slightly reduced velocity as compared to immobilized Myo1b (Fig. 3C, Table S1). This is in line with the results by Grover et al *(20)* showing a decreased gliding velocity of membrane-anchored kinesins due to their slippage in the lipid bilayer.

In these experimental conditions, we observed a significant increase of the actin depolymerization rate at the barbed end k_{off} when filaments slide on Myo1b bound to a SLB, although weaker than for immobilized Myo1b, while keeping the polymerization rate unchanged (Fig. 3E, Fig. 3F and Table S2). We conclude that the dissipation of sliding filaments in SLBs is low enough to let Myo1b exert a significant dissociation force even when bound to a fluid membrane (See force balance in Fig. 3G).

In summary, we have shown that the sliding of actin filaments on catch-bond motors induces an increase of the actin dissociation rate k_{off} at the barbed-end which depends on the gliding velocity (Tables S1 and S2). In contrast, muscle Myosin II which is a weak catch-bond *(13)* in the pN force range, does not affect actin polymerization dynamics, although filament sliding on Myosin II is much faster. Different actin-binding proteins are already known for preventing actin polymerization (capping protein) *(12)*, enhancing it (formin) *(21, 22)* or depolymerizing actin (ADF/cofilin) *(23, 24)* at the barbed end. Some kinesin motors, e.g., kinesins 8 and 13, have been shown to depolymerize microtubules *(25, 26)*. However, this is the first time that a myosin motor is reported to affect actin filament growth. Note that the catch bond effect on the actin dissociation rate is in part due to the longer attachment time of the Myo1b motor, other mechanisms that increase the duty ratio would potentially lead to a similar effect on actin dissociation. Moreover, the molecular mechanisms of dissociation due to Myo1b are not known and one cannot exclude that dissociation may be partly due to molecular mechanisms. Another Myosin 1 (Myosin 1c) that is also a catch-bond, might regulate actin dynamics at the barbed-end. However, the lifetime of its attachment to actin under load is ten times lower than for Myo1b *(27)*, thus we expect its impact on actin dynamics to be moderate as compared to Myo1b, but this remains to be tested.

Experimental evidence supports a role of several Myosin 1 proteins in membrane remodeling *(3)*. Similarly to capping proteins *(28)*, Myo1b and perhaps other Myosin 1 proteins could shape membranes by regulating the growth of filaments at the plasma membrane. Alternatively, Myo1b could shape membranes by inducing stresses in the cortical actin. Indeed, Myo1b induces actin movement and reduces actin growth when bound to supported bilayers, as shown in our experiments. Since the fluidity of our synthetic membranes and of cellular membranes are similar (Fig. 3A), we propose that Myo1b has the same function in cells. Collectively, these motors could drive the sliding of actin filaments at the membrane surface, which could create stresses that relax by deforming the cortex and the attached membrane. Interestingly, when Myo1b is bound to a deformable giant liposome, we observed that it produces membrane invaginations in presence of stabilized actin filaments (Fig. S5).

bioRxiv preprint doi: https://doi.org/10.1101/375923; this version posted July 24, 2018. The copyright holder for this preprint (which was not certified by peer review) is the author/funder. All rights reserved. No reuse allowed without permission.

Myo1b's influence on actin dynamics can control the organization of actin networks, as reported in growth cones (6). An actin network can be impacted by Myo1b in different ways. It can reduce the length of actin filaments, as shown by this work, and thus change the mesh-size, or the cortical thickness and consequently the cortical contractibility (29). Whether or not it can affect the Arp2/3-dependent branched actin network and/or formin-dependent actin bundles remains to be explored. Moreover, since Myo1b is specifically present at the interface between the plasma membrane and the cortical actin, Myo1b may coordinate receptor signaling by arranging the cytoskeleton (30).

Besides Myosin II and Myosin 1 proteins, Myosin VI has also been reported to influence the actin architecture during, e.g. spermatid individualization in Drosophila (31) or around melanosomes (32). It might be time now to take a fresh look on the involvement of non-conventional myosins in actin dynamics and organization.

References

1. D. V. Köster, S. Mayor, *Curr. Opin. Cell Biol.* **38**, 81 (2016).
2. S. Pyrpassopoulos *et al.*, *Sci. Rep.* **6**, 25524 (2016).
3. B. B. McIntosh, E. M. Ostap, *J. Cell Sci.* (2016).
4. C. G. Almeida *et al.*, *Nat. Cell Biol.* **13**, 779 (2011).
5. P. Gupta *et al.*, *Biol. Open* **2**, 1288 (2013).
6. Iuliano *et al.*, *J. Cell Biol.* **217**, 2033 (2018).
7. M. Joensuu *et al.*, *Mol. Biol. Cell* **25**, 1111 (2014).
8. M. J. Greenberg, T. Lin, Y. E. Goldman, H. Shuman, E. M. Ostap, *Proc. Natl. Acad. Sci. USA* **109**, E2433 (2012).
9. J. M. Laakso, J. H. Lewis, H. Shuman, E. M. Ostap, *Science* **321**, 133 (2008).
10. J. H. Lewis, T. Lin, D. E. Hokanson, E. M. Ostap, *Biochemistry* **45**, 11589 (2006).
11. T. Guérin, J. Prost, J.-F. Joanny, *The European Physical Journal E* **34**, 60 (2011).
12. M. F. Carlier *et al.*, *Cell. Mol. Life Sci.* **72**, 3051 (2015).
13. C. Veigel, J. E. Molloy, S. Schmitz, J. Kendrick-Jones, *Nat. Cell Biol.* **5**, 980 (2003).
14. A. H. Crevenna *et al.*, *eLife* **4**, e04599 (2015).
15. A. Yamada *et al.*, *Nat. Commun.* **5**, 3624 (2014).
16. M. J. Footer, J. W. Kerssemakers, J. A. Theriot, M. Dogterom, *Proc. Natl. Acad. Sci. USA* **104**, 2181 (2007).
17. S. Komaba, L. M. Coluccio, *J. Biol. Chem.* **285**, 27686 (2010).
18. L. Guo *et al.*, *ChemPhysChem* **9**, 721 (2008).
19. S. Pyrpassopoulos, E. A. Feeser, J. N. Mazerik, M. J. Tyska, E. M. Ostap, *Curr. Biol.* **22**, 1688 (2012).
20. R. Grover *et al.*, *Proc. Natl. Acad. Sci. USA* **113**, E7185 (2016).
21. D. R. Kovar, J. R. Kuhn, A. L. Tichy, T. D. Pollard, *J. Cell Biol.* **161**, 875 (2003).
22. S. Romero *et al.*, *Cell* **119**, 419 (2004).
23. A. B. Johnston, A. Collins, B. L. Goode, *Nat. Cell Biol.* **17**, 1504 (2015).
24. H. Wioland *et al.*, *Curr. Biol.* **27**, 1956 (2017).
25. V. Varga, C. Leduc, V. Bormuth, S. Diez, J. Howard, *Cell* **138**, 1174 (2009).
26. C. A. Moores, R. A. Milligan, *J. Cell Sci.* **119**, 3905 (2006).
27. Michael J. Greenberg, G. Arpağ, E. Tüzel, E. M. Ostap, *Biophys. J.* **110**, 2568 (2016).
28. K. Dürre *et al.*, *Nat. Commun.* **9**, 1630 (2018).
29. H. Ennomani *et al.*, *Curr. Biol.* **26**, 616 (2016).
30. S. A. Freeman *et al.*, *Nat. Commun.* **6**, 6168 (2015).
31. T. Noguchi, M. Lenartowska, K. G. Miller, *Mol. Biol. Cell* **17**, 2559 (2006).

bioRxiv preprint doi: https://doi.org/10.1101/375923; this version posted July 24, 2018. The copyright holder for this preprint (which was not certified by peer review) is the author/funder. All rights reserved. No reuse allowed without permission.

32. S. Loubéry, C. Delevoye, D. Louvard, G. Raposo, E. Coudrier, *Traffic* **13**, 665 (2012).
33. C. Ciobanasu, B. Faivre, C. Le Clainche, *Nat. Commun.* **5**, 3095 (2014).
34. W. J. Galush, J. A. Nye, J. T. Groves, *Biophys. J.* **95**, 2512 (2008).
35. B. Sorre *et al.*, *Proc. Natl Acad. Sci. USA* **109**, 173 (2012).
36. D. M. Soumpasis, *Biophys. J.* **41**, 95 (1983).
37. A. Weinberger *et al.*, *Biophys. J.* **105**, 154 (2013).
38. M. J. Greenberg, E. M. Ostap, *Trends Cell Biol.* **23**, 81 (2013).
39. T. A. J. Duke, *Proc. Natl Acad. Sci. USA* **96**, 2770 (1999).
40. E. Bengtsson *et al.*, *Biophys. J.* **111**, 1465 (2016).
41. A. Mogilner, G. Oster, *Biophys. J.* **84**, 1591 (2003).
42. A. Vilfan, E. Frey, F. Schwabl, *Europhys. Lett.* **45**, 283 (1999).
43. P. G. Saffman, M. Delbrück, *Proc. Natl Acad. Sci. USA* **72**, 3111 (1975).
44. P. F. Almeida, W. L. Vaz, in *Handbook of Biological Physics* R. Lipowsky, E. Sackmann, Eds. (Elsevier, Amsterdam, 1995), vol. 1, pp. 305-357.

Acknowledgments
We thank B. Goud for insightful discussions, C. Le Clainche (I2BC, Gif-sur-Yvette, France) for providing actin and Myosin II and critically reading the manuscript, F.-C. Tsai for SLB preparation, L. Blanchoin, C. Leduc, J. Prost, M. Henderson for carefully reading the manuscript. The authors greatly acknowledge the Cell and Tissue Imaging (PICT-IBiSA), Institut Curie, member of the French National Research Infrastructure France-BioImaging (ANR10-INBS-04). This work was supported by Institut Curie, Centre National de la Recherche Scientifique (CNRS), the European Research Council (ERC) (J.F.J., P.B. and E.C are partners of the advanced grant, project 339847 and their groups belong to the CNRS consortium CellTiss, the Labex CelTisPhyBio (ANR-11-LABX0038) and Paris Sciences et Lettres (ANR-10-IDEX-0001-02). J.P. and R.K. were funded by the ERC project 339847.

List of Supplementary Materials
- Material and Methods
- Supplementary text (Detailed theoretical model)
- Tables S1 and S2
- Figures S1-S5
- Movies S1-S11

bioRxiv preprint doi: https://doi.org/10.1101/375923; this version posted July 24, 2018. The copyright holder for this preprint (which was not certified by peer review) is the author/funder. All rights reserved. No reuse allowed without permission.

Figure Legends

Figure 1: **Schemes of Myo1b-Actin gliding assays**. **(A)** Schematic representation of domain organization of Myo1b. Motor domain (blue); LCBD domain (yellow); TH1 domain (red), PH domain (cyan) that binds phosphoinositides. **(B**) Myo1b conformational changes during actin gliding. An individual motor (colored) along the filament exerts a propulsive force for a "time of attachment" $< \frac{d}{v_f}$, while for $\tau > \frac{d}{v_f}$ the filament experiences a resistive force, slowing down its motion. In this later stage, the motor detaches with a force dependent rate $\omega_{det}(F)$. **(C)** Schematic representations of gliding assays of stabilized actin filaments (I-II) and polymerizing actin filaments (III-IV) sliding on Myo1b anchored on coverslip (I-III) or bound to a supported lipid bilayer (II-IV).

Figure 2: **Sliding on immobilized Myosin 1b increases F-actin depolymerization. (A)** Representative kymographs of stabilized F-actin (top) or polymerizing F-actin with 0.6 µM G-actin (bottom), on uncoated glass (movie S6) or sliding on glass coated with Myo1b (2 mM and 0.2 mM ATP, see movies S3 and S4) or Myosin II (see movie S9). The sliding distance ΔX and the elongation ΔL of the filaments are indicated by white arrows. Actin fluorescence intensity is represented according to the "Fire" LUT of Image J. Scale bar, 5µm. 1 image/10 sec. **(B)** Distributions of the sliding velocities v_f of stabilized (top) and polymerizing actin filaments (bottom) on immobilized Myo1b at about 8000 molecules/µm^2 (at 2 mM (blue) and 0.2 mM ATP (grey)) or Myosin II (orange). (**C**) Filament elongation ΔL (normalized by the length of the actin subunit (su) equal to 2.7 nm) versus time for filaments shown in A (bottom) in the absence of myosins and in the presence of Myosin II or Myo1b at two ATP concentrations. Polymerization rate at the barbed end v_p is deduced from the slope. **(D)** v_p as a function of G-actin concentration C_m for the different conditions. The fits correspond to $v_p = k_{on}C_m - k_{off}$, with k_{on} the rate of association of G-actin and k_{off} the rate of dissociation. C_{c+} is the critical concentration for polymerization. Inset: k_{off} for the different conditions. Error bars represent s.e.m. (n>30). **(E)** Model for the role of Myo1b motor on the dissociation (depolymerization) rate k_{off}. The filament, sliding at velocity v_f, experiences a force F_{fil} at the barbed end while the motor is attached, thus impacting k_{off}, but not the association (polymerization) rate k_{on}.

Figure 3: **Sliding on Myosin 1b bound to a supported lipid bilayer increases F-actin depolymerization (A)** Top: Diffusion coefficients of Atto488DOPE (DOPE*) and Alexa488-labelled Myo1b (Myo1b*) in a SLB with bound Myo1b and in absence or in the presence of a dense F-actin network (n = 30). Bottom: Effective diffusion coefficients of Cherry-CAAX, Cherry-Myo1b, expressed in HEK293T cells (n > 5). Error bars represent s.e.m. **(B)** Representative kymographs of non-polymerizing (top) and polymerizing F-actin (bottom) in the presence of 0.6 µM G-actin with Myo1b bound to SLBs (movie S11). Scale bar, 5µm. 1image/10 sec. **(C)** Comparison of the distribution of the velocities v_f of stabilized (top) and polymerizing F-actin (bottom) sliding on immobilized Myo1b (dark blue) or on Myo1b bound to a SLB (cyan). **D)** Model for filament sliding: The effective filament sliding is determined by a balance between the viscous dissipation of the motor moving with a velocity v_m in the lipid bilayer with a viscosity η_m and a filament sliding at a velocity $\widetilde{v_f}$ in a solution of viscosity η_b. **(E)** ΔL versus time for the single filaments shown in (B). **(F)** v_p as a function of G-actin concentration C_m for the different conditions. The fit to the data is the same as in Fig. 2D. Inset: k_{off} for the different conditions. Error bars represent s.e.m. (n>25). **(G)** Model for

bioRxiv preprint doi: https://doi.org/10.1101/375923; this version posted July 24, 2018. The copyright holder for this preprint (which was not certified by peer review) is the author/funder. All rights reserved. No reuse allowed without permission.

force transmission: The effective force experienced by the polymerizing filament $\widetilde{F_{fil}}$ is diminished by the motion in the lipid bilayer of the motor v_m at the barbed end.

bioRxiv preprint doi: https://doi.org/10.1101/375923; this version posted July 24, 2018. The copyright holder for this preprint (which was not certified by peer review) is the author/funder. All rights reserved. No reuse allowed without permission.

Figure 1

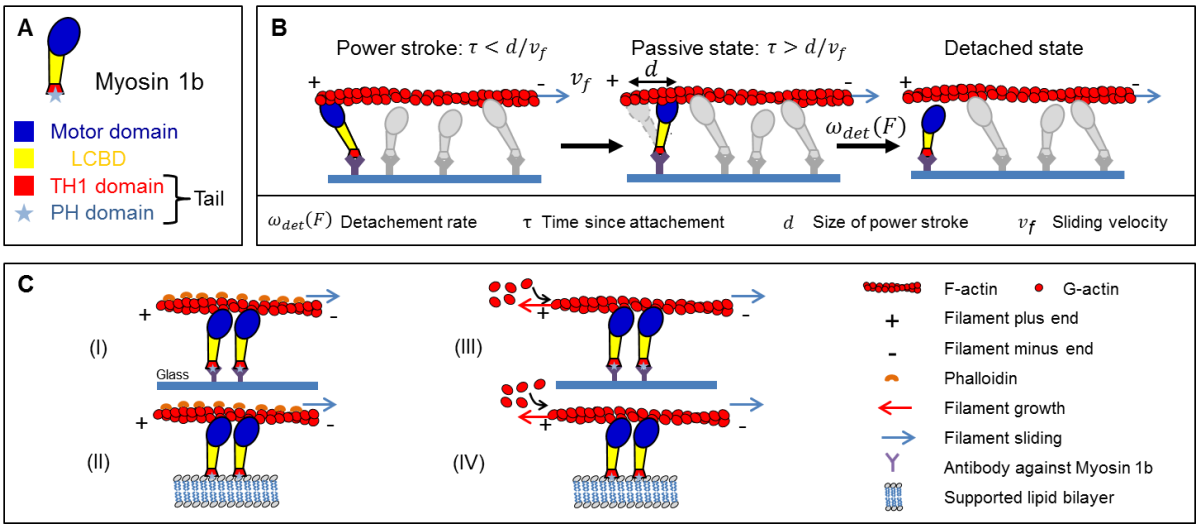

bioRxiv preprint doi: https://doi.org/10.1101/375923; this version posted July 24, 2018. The copyright holder for this preprint (which was not certified by peer review) is the author/funder. All rights reserved. No reuse allowed without permission.

Figure 2

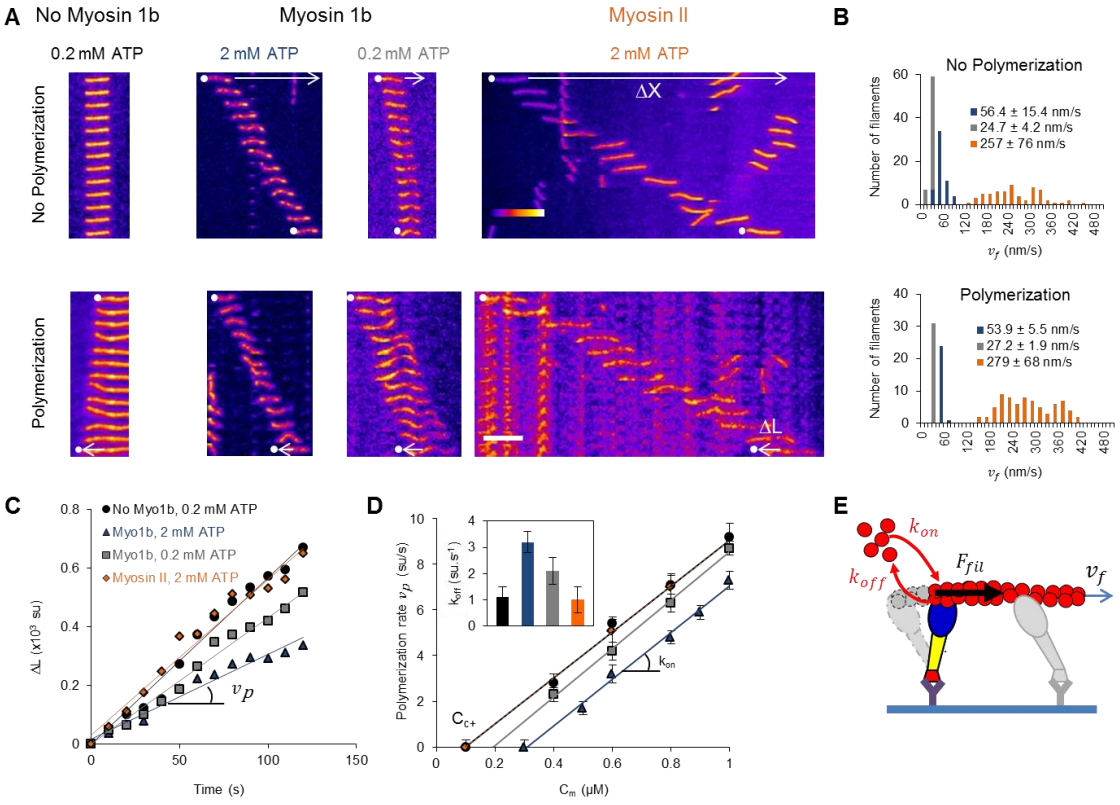

bioRxiv preprint doi: https://doi.org/10.1101/375923; this version posted July 24, 2018. The copyright holder for this preprint (which was not certified by peer review) is the author/funder. All rights reserved. No reuse allowed without permission.

Figure 3

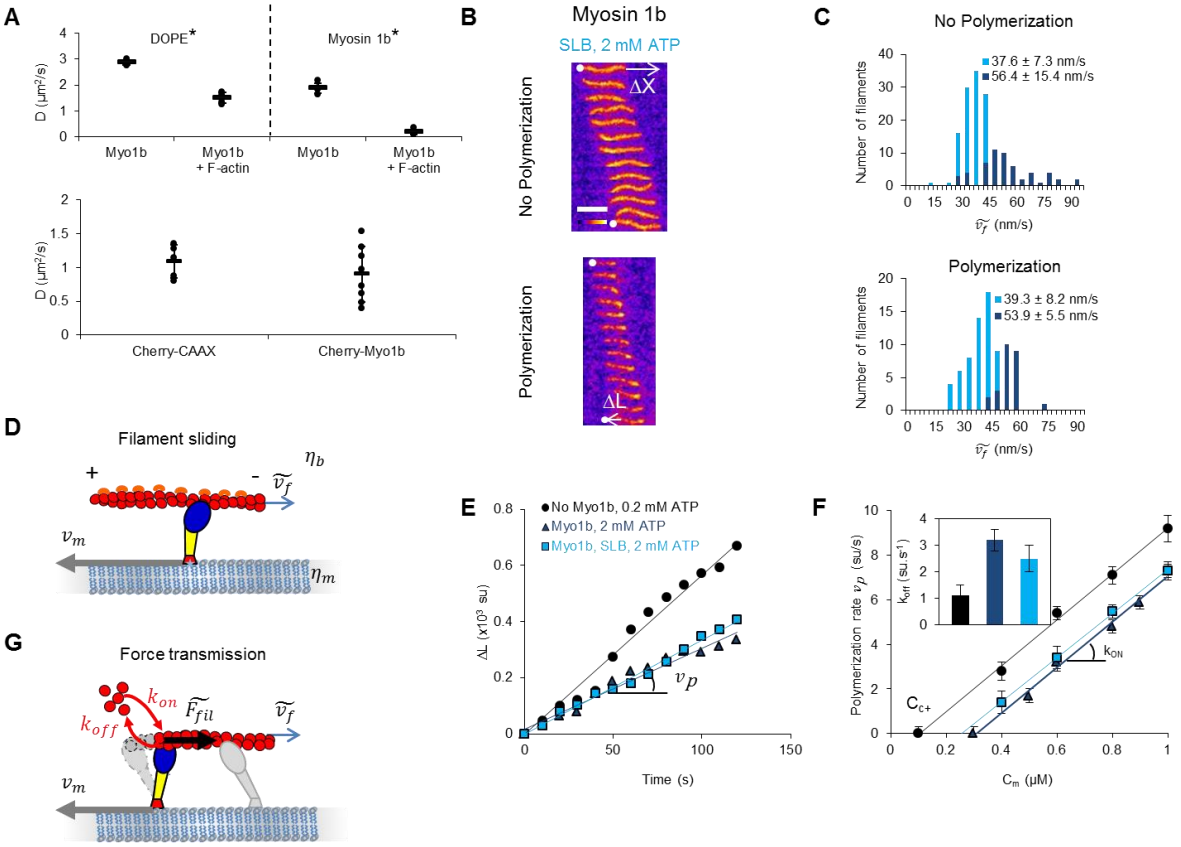

bioRxiv preprint doi: https://doi.org/10.1101/375923; this version posted July 24, 2018. The copyright holder for this preprint (which was not certified by peer review) is the author/funder. All rights reserved. No reuse allowed without permission.

Supplementary Materials

Materials and Methods

Protein purification

Actin was purified from rabbit muscle and isolated in monomeric form in G buffer (5 mM Tris-HCl, pH 7.8, 0.1 mM $CaCl_2$, 0.2 mM ATP, 1 mM DTT and 0.01% NaN_3). Actin was labeled with Alexa 594 succimidyl ester-NHS (*33*).

Expression and purification of Myosin 1b: FLAG-myo1b was expressed in HEK293-Flp-In cells cultured in Dulbecco's modified Eagle medium supplemented with 10% fetal bovine serum and 0.18 mg ml^{-1} hygromycine in a spinner flask at 37 °C under 5% CO_2, and collected by centrifugation (1,000 g, 10min, 4 °C) to obtain a 4–5 g of cell pellet. The pellet was lysed in FLAG Trap binding buffer (30 mM HEPES, pH 7.5, 100 mM KCl, 1 mM $MgCl_2$, 1mM EGTA, 1 mM ATP, 1 mM DTT, 0.1% protease inhibitor cocktail (PIC), 1% Triton X-100) for 30 min at 4 °C and centrifuged at 3,400 g for 10 min at 4 °C. The collected supernatant was then ultracentrifuged (250,000 g, 60 min, 4 °C). The solution between pellet and floating lipid layer was incubated with 150 µl of anti-FLAG beads for 2 h at 4 °C. The beads were collected by centrifugation (1,000 g, 5 min, 4 °C). After a washing step, FLAG-myo1b was then eluted by incubating with 0.24 mg ml^{-1} of 3X FLAG peptide in 300 µl elution buffer (binding buffer without Triton X-100 supplemented with 0.1% methylcellulose) for 3 h at 4 °C. After removal of the beads by centrifugation (1,000 g, 3 min, 4 °C), the protein solution was dialyzed against elution buffer overnight at 4 °C to remove the 3X FLAG peptide. Myo1b was fluorescently labeled using Alexa Fluor 488 5-SDP ester (*15*). Inactivated Myo1b was removed by ultracentrifugation (90,000 rpm, 20 min, 4 °C) with 1 µM F-actin in presence of 2 mM ATP.

Supported lipid bilayer (SLB) preparation

SLBs were formed by fusion of small unilamellar vesicles (SUVs) prepared as follows. Lipid mixtures containing 79.5 % POPC, 20 % L-α-phosphatidylinositol-4,5-bisphosphate ($PI(4,5)P_2$) and 0.5 % Rhodamine-PE or Atto488-DOPE (mol/mol) were mixed together in a glass vial, dried with N_2, placed in vacuum desiccator for 1 hour, then rehydrated with Fluo F buffer (5 mM Tris-HCl- pH 7.8, 100 mM KCl, 1 mM $MgCl_2$, 0.2 mM EGTA, 0.2 mM or 2 mM ATP, 10 mM DTT, 1 mM DABCO, 0.01% NaN_3) for 30 min at room temperature, to a final lipid concentration of 2 mM. After rehydration, the glass vial was vortexed to detach the liposomes. SUVs were formed by sonication, aliquoted and stored at -20 °C. For SLB formation by fusion, $CaCl_2$ was added to a final concentration of 5 mM, with 50 µl of SUVs. The solution was incubated in the chamber for 20 min and washed 5 times with Fluo F buffer 0.1 % BSA. The quality of the SLB was checked by FRAP.

Single-filament TIRF microscopy assays

The kinetics of single filament assembly was monitored by TIRF microscopy (Eclipse Ti inverted microscope, 100X TIRF objectives, Quantem 512SC camera). The experiments were controlled using the Metamorph software. Coverslips and glass slides were sequentially cleaned by sonication with H_2O, ethanol, acetone for 10 min, then 1M KOH for 20 min and H_2O for 10 min. In the case of supported lipid bilayer, first the coverslips and glass slides were cleaned by sonication with Hellmanex III (Hellma Analytics) for 30 min. Flow chambers were assembled with a coverslip bound to a glass slide with two parallel double-stick tapes. The chamber was incubated with 100 nM anti-myo1b antibody in G buffer (5 mM Tris-HCl, pH 7.8, 0.1 mM $CaCl_2$, 0.2 mM ATP, 1 mM DTT and 0.01% NaN_3) for 10 min at room temperature. The chamber was rinsed three times with buffer G 0.1 % BSA and incubated 5 min at room temperature. Then the chamber was incubated with 300 nM Alexa488-labeled myo1b in Fluo F buffer (5 mM Tris-HCl, pH 7.8, 100 mM KCl, 1 mM

bioRxiv preprint doi: https://doi.org/10.1101/375923; this version posted July 24, 2018. The copyright holder for this preprint (which was not certified by peer review) is the author/funder. All rights reserved. No reuse allowed without permission.

$MgCl_2$, 0.2 mM EGTA, 0.2 mM or 2 mM ATP, 10 mM DTT, 1 mM DABCO, 0.01% NaN_3) for 10 min at room temperature. Assays were performed in Fluo F buffer, containing 0.2 or 2 mM constant ATP, supplemented with 0.3% methylcellulose (Sigma) and with G-actin (10 % Alexa594) or F-actin (stabilized with phalloidin-Alexa594) at indicated concentrations. To maintaining a constant concentration of ATP in this assay an ATP regenerating mix, including 2 mM ATP, 2 mM $MgCl_2$, 10 mM creatine phosphate and 3.5 U/mL creatine phosphokinase, which constantly re-phosphorylates ADP into ATP to maintain a constant concentration of free ATP, was added.

The sliding and elongation velocities of actin filaments were analyzed by using Kymo Tool Box plugin of Image J software (available from fabrice.cordelieres@curie.upsud.fr). We consider that each actin subunit contributes to 2.7 nm of the filament length.

Myosin 1b surface density

We measured the protein surface density (number of proteins per unit area) on solid surfaces or on SLBs by using a previously established procedure (*34*, *35*). It is calculated from a labeled proteins/lipids calibration. We first measure the fluorescence of POPC SLBs containing predefined amounts of Atto488-DOPE fluorescent lipids (DOPE*) to establish the relationship between the density of DOPE* n_{DOPE*} and the corresponding fluorescence intensity I^{SLB}_{DOPE*} (Fig. S1Ba). Assuming an area per POPC of 0.68 nm^2, we derive the calibration coefficient A corresponding to the slope of this curve. Note that A depends on the illumination and recording settings of the microscope .

$$n_{DOPE*} = A \times I^{SLB}_{DOPE*}$$

Since Myo1b is labeled with Alexa488 and not Atto488, we have to correct this value by the ratio of fluorescence of the two fluorescent dyes in bulk deduced from the slope of the titration curves $\frac{I_{Alexa488}}{I_{DOPE^*}}$ (Fig. S1Bb and c). We then obtained the surface density of the protein deduced from the measurement of the Myo1b-Alexa488 intensity I_{Myo1b*} as:

$$n_{Myosin\ 1B} = \frac{A}{\frac{I_{Alexa488}}{I_{DOPE^*}} \times n^*} \times I_{Myo1b*}$$

where n^* is the degree of labeling for the protein of interest (1). In our experiments, the calibration factor $\frac{A}{\frac{I_{Alexa488}}{I_{DOPE^*}} \times n^*}$ is equal to 0.278.

FRAP methods

For diffusion measurements, Fluorescence Recovery After Photobleaching (FRAP) experiments were performed through a X100 or X60 oil immersion objective on an inverted spinning disk confocal microscope (Nikon eclipse Ti-E equipped with a Prime 95B™ Scientific CMOS camera, Photometrics) equipped with a FRAP unit. Recovery curves (average of 5 independent experiments, performed on different circular regions of the SLB using the same bleaching conditions) were normalized to the initial intensity and fitted with a single exponential function. We derive the $\tau_{1/2}$ time corresponding to the time at which the fluorescence signal has recovered 50% of its value before bleach. We calculated the diffusion coefficient using the Soumpasis equation (*36*):

$D_r = 0.224 \frac{r^2}{\tau_{1/2}}$, where r is the radius of the bleach region.

Giant unilamellar vesicle (GUV) preparation

Lipid compositions for GUVs were 79.7 % POPC, 20 % L-α-phosphatidylinositol-4,5-bisphosphate ($PI(4,5)P_2$) and 0.3 % Texas Red DHPE. GUVs were prepared by using

bioRxiv preprint doi: https://doi.org/10.1101/375923; this version posted July 24, 2018. The copyright holder for this preprint (which was not certified by peer review) is the author/funder. All rights reserved. No reuse allowed without permission.

polyvinyl alcohol (PVA) gel-assisted method in a 200 mM sucrose buffer at room temperature for 2 hour as described previously (*37*).

Theoretical model for filament sliding

Myosin1b as a catch bond motor: Myosin 1b is identified as a molecular motor with a catch-bond detachment rate, i.e., it responds to small resisting loads by dramatically increasing its duty ratio (*9, 38*). While its binding rate to actin is independent of the applied force ($\omega_b = 0.38s^{-1}$ at an ATP concentration of $C_{ATP} = 50\mu M$), its unbinding rate does decrease with applied force, F,

$$\omega_{det}(F) = \omega_0 \exp\left(-\frac{Fb}{KT}\right) + \omega_i. \qquad \text{(SE 1)}$$

Here ω_i is the force independent unbinding rate, ω_0 the force-dependent unbinding rate and b, the distance quantifying the strain sensitivity of the motor (at $C_{ATP} = 50\mu M$ the reported values are: $\omega_i = 0.02s^{-1}$, $\omega_0 = 1.6s^{-1}$ and $b = 12nm$ (*9*)). In a crossbridge model, an actin filament is transiently attached to the myosin motor, exerting a force F_{mot}:

$$F_{mot} = k_c(-d + v_f\tau). \qquad \text{(SE 2)}$$

Here, $d = 8.4\ nm$ is the power stroke, v_f is the sliding speed of the filament and τ the age of the motor (the time since attachment to the actin filament). The cross-bridge stiffness is $k_c = 0.2pN/nm$ (note that this value was determined for myosin 1c and does not vary widely between different motor species and that the exact numerical value does not change our results qualitatively, e.g. for Myosin 2, $k_c = 0.4pN/nm$).

Two-state cross-bridge model with ATP dependence: To describe the actin filament sliding over Myosin1b motors and to include the explicit ATP dependence we invoke a modified two-state cross-bridge model. This model is extensively discussed in Guérin et al. (*11*) and is valid for a filament sliding at stationary velocity v_f and in the limit of a large number of molecular motors propelling the filament. To include the effect of ATP concentration, we consider two populations of molecular motors, the "active", $\rho_a(\tau)$ (ATP bound) and "passive" motors, $\rho_p(\tau)$ (not bound to ATP) (See Fig. S3A). The total number of attached motors, $n_a = 1 - n_d$, equals the sum of the two populations,

$$\int_0^\infty \rho_a(\tau) + \rho_p(\tau)d\tau = 1 - n_d, \qquad \text{(SE 3)}$$

where, n_d is the total fraction of detached motors. The binding rate of the motor to the filament, ω_b, enters the equation through the initial condition $\rho_a(0) = \xi\omega_b n_d$ and $\rho_p(0) = (1-\xi)\omega_b n_d$. Here ξ is the fraction of motors that are bound to an ATP molecule and thus are able to perform a power-stroke. The active fraction ξ saturates for sufficiently large values of the ATP concentration and since a single ATP molecule is required for the motor cycle, it should follow a Michaelis-Menten equation,

$$\xi = \frac{C_{ATP}}{C_{ATP}+\xi_0}, \qquad \text{(SE 4)}$$

where $\xi_0 \approx 1mM$ is the value above which the ATP concentration starts to saturate (*39, 40*). The linear densities of attached motors, both for the active, $\rho_a(\tau)$, as well as for the passive motors, $\rho_a(\tau)$, as function of the age, τ, evolves as,

$$\partial_\tau\rho_a(\tau) = -\omega_{det}(F_{mot})\rho_a(\tau), \qquad \text{(SE 5)}$$
$$\partial_\tau\rho_p(\tau) = -\omega_{det}(F_{mot})\rho_p(\tau). \qquad \text{(SE 6)}$$

Here $\omega_{det}(F_{mot})$ is the force dependent detachment rate given by Eq. SE 1. Note that under saturated ATP conditions, $\rho_a = 1$ and $\rho_p = 0$.

bioRxiv preprint doi: https://doi.org/10.1101/375923; this version posted July 24, 2018. The copyright holder for this preprint (which was not certified by peer review) is the author/funder. All rights reserved. No reuse allowed without permission.

The time-averaged force exerted by a single molecular motor along the filament is given by the sum of the contribution of the "passive" motors (always negative) and that of the "active" motors,

$$F_{mot} = -k_c\left(\int_0^\infty \left(-d + v_f\tau\right)\rho_a(\tau)d\tau + \int_0^\infty v_f\tau\rho_p(\tau)d\tau\right), \qquad \text{(SE 7)}$$

where k_c is the crossbridge stiffness of the motor and d is the power stroke. The total force on the filament is obtained by multiplying this force by the total number of motors N. In Fig. S3B we show, as function of the age, τ, that the active motors (solid curve) initially perform a positive propulsive force due to the power-stroke, followed by a negative, frictional force. For the active motors, we therefore identify two regimes while the motor is attached to the filament: while $\tau < d/v_f$, the motor performs its power stroke and thus exerts a positive force on the filament, while for $\tau > d/v_f$, the motor acts as a resistive spring, slowing down the sliding of the filament (See solid curve Fig. S3B). The passive motors only display the frictional force (dashed curve). To calculate the total frictional part of the force included in the first term, the first integral (active motors) of Eq. SE 7 has to be taken from $d/v_0$to ∞ , i.e.,

$$F_{fric} = -k_c\left(\int_{d/v_0}^\infty \left(-d + v_f\tau\right)\rho_a(\tau)d\tau + \int_0^\infty v_f\tau\rho_p(\tau)d\tau\right). \qquad \text{(SE 8)}$$

To directly compare our model with the experiments we have to identify the binding and unbinding rates at the relevant ATP concentrations. The values for the (un)-bindings kinetics reported in (*9*) are obtained at significantly lower ATP concentrations than reported here. Therefore, we rescale the binding and unbinding rates to match the sliding velocity at the experimental ATP concentration, while keeping the duty ratio unaltered (*10*). We linearly rescale these kinetic parameters (obtained in different range of ATP values) with a numerical factor of 80 to recover the experimentally observed sliding speed at saturated ATP concentration ($v_f \approx 55\,nm/s$ for $C_{ATP} = 2mM$), keeping all the ratios or detachment/attachment rates constant. In Table SI1, we outline the values of all the parameters used here. Note that altering the numerical values used here does not qualitatively alter the presented results. At non-saturated ATP concentrations only a fraction of the total available motors along the filament are able to perform a power-stroke. This is included in the model by considering the two populations of molecular motors along the filament, (1) motors binding an ATP molecule perform a power-stroke, exerting a positive force, and (2) motors failing to bind an ATP attach to the filament but do not perform a power-stroke (Fig. S3A). If we compare the force-velocity relations for a catch-bond motor (Eq. SE 1) and a motor with a force-independent detachment rate, at otherwise identical conditions ($\omega_{det}(F) = \omega_0$) we find that the sliding velocity at vanishing external force is significantly reduced as a result of the catch bond characteristic of the motor (Fig. S3C).

Lowering the ATP concentration from saturated conditions $C_{ATP} = 2mM$ to $C_{ATP} = 0.2mM$ decreases the sliding velocity of the filament from $v_f \approx 55\,nm/s$ to $v_f \approx 43.5\,nm/s$ (Fig. S3D). This diminished sliding velocity is due to the fact that, upon lowering the ATP concentration, fewer motors are able to bind an ATP molecule and hence less motors contribute to the propulsion of the filament (Fig. S3E). Note that for the detachment rate we did not include any further explicit ATP dependence. At lower ATP concentrations the (un)binding rates of actin and motor may be further impacted by the ATP, which will further lower the sliding speed of the filament. This additional effect, however, is not taken into account in our model and would require an additional unknown parameter.

bioRxiv preprint doi: https://doi.org/10.1101/375923; this version posted July 24, 2018. The copyright holder for this preprint (which was not certified by peer review) is the author/funder. All rights reserved. No reuse allowed without permission.

*Table SI1: Numerical values of the cross-bridge model. * note that the ratio's of these values have been chosen identical to those determined in (9); however they have all been rescaled to match the current ATP conditions and sliding speed.*

Symbol	Value	Description
ω_i	$1.7\ s^{-1}$	Strain independent detachment rate*
ω_0	$134 s^{-1}$	Strain dependent detachment rate*
ω_b	$32\ s^{-1}$	Attachment rate*
d	$8.4\ nm$	Size of the power stroke
b	$12\ nm$	Strain sensitivity of the motor
k_c	$0.2\ pN/nm$	Cross-bridge stiffness of motor complex

Force dependence of the depolymerization rate: The actin filaments sliding over an array of Myo1b motors experiences an increased friction force due to the longer attachment time of the motor/filament complex. The longer attachment time of the Myo1b motor at the barbed end induces a transient stress in the filament, enhancing the depolymerization. Experimentally (Fig. 2D), we show that, while the polymerization rate remains unaltered for filaments sliding over Myo1b, the depolymerization rate of the actin filament increases. We hypothesize that this effect can be described by the average force dependent depolymerization rate (*41*),

$$k_d(F_{fric}) = k_d^0\left(n_d + \int_0^\infty \rho_a(\tau)\exp\frac{k_c(-d+v_f\tau)}{F^*}d\tau + \int_0^\infty \rho_p(\tau)\exp\frac{k_c(v_f\tau)}{F^*}\,d\tau\right) \quad \text{(SE 9)}$$

where k_d^0 is the depolymerization rate in the absence of an applied force and F^* is the characteristic scale for the force sensitivity of the depolymerization rate of the actin. Since the motor assay on which the filaments slide contain catch-bond motors, the effective friction force on the filament is increased, enhancing the force at the plus-end and hence the depolymerization. First we calculate the time averaged friction force using Eq. SE 8 and find that $F_{mot} \approx 0.5pN$ for $C_{ATP} = 2mM$ and $F_{mot} \approx 0.2pN$ for $C_{ATP} = 0.2m$. Using Eq. SE 9 we estimate the predicted decrease in depolymerization rate as a function of ATP concentration for various values of the characteristic force, F^* (Fig. S4A) and find that increasing the ATP concentration, increases the friction force between the filament and the motor and hence increases the depolymerization rate. Note also that, depending on F^* this depolymerization rate may diverge in our theoretical model. Alternatively, if we increase the distance parameter quantifying the strain sensitivity of the motor (b in Eq. SE 1) we find that the impact on the depolymerization rate decreases, pointing at the important role of the catch bond characteristic in this process.

To compare with a conventional, force-independent motor, we also calculated the time averaged force for a Myosin II motor where we have, similarly to the Myosin 1b rescaled the binding/unbinding rates to match the sliding velocity of the experimental conditions, while keeping their ratio constant ($k_c = 0.4pN/nm$, $d = 5\ nm$, $\omega_0 = 0\ s^{-1}$, $\omega_b = 71.4s^{-1}$ and $\omega_i = 1.4\ s^{-1}$ since Myosin II does not have the catch bond characteristics). At a velocity $v_f \approx 250nm/s$ we obtain a time averaged frictional force $F_f \approx 0.025pN$, which is roughly an order of magnitude smaller compared to that of Myosin 1b, confirming the importance of the catch bond characteristic of the motor for the depolymerization.

Taken together our model shows two interesting features, first, since the filaments are sliding on (catch bond) Myo1b motors, their sliding speed decreases while the effective friction exerted by the motor on the filament increases. Increasing the sliding velocity by e.g. increasing the ATP concentration increases the time that the motor spends under tension, hence the total friction force experienced by the filament and hence enhances the depolymerization further, until we reach saturation of ATP.

bioRxiv preprint doi: https://doi.org/10.1101/375923; this version posted July 24, 2018. The copyright holder for this preprint (which was not certified by peer review) is the author/funder. All rights reserved. No reuse allowed without permission.

Filament sliding on a lipid bilayer: To estimate how the motor force is transmitted to the filament when the molecular motors are immersed in a lipid bilayer, instead of rigidly anchored to a solid surface, we write down a simplified force balance between the viscous friction force of the motor/filament and the force exerted by the molecular motor f_{mot}, i.e.,

$$-\xi_f \tilde{v}_f = n f_{mot}, \quad \text{(SE 10)}$$

$$\xi_f \tilde{v}_f = -n \xi_m v_m, \quad \text{(SE 11)}$$

where $n = \rho * l$ is the number of attached motors along the filament (l is the filament length), ξ_m is the in-plane friction coefficient of the motor complex in the lipid bilayer, v_m , the speed of a molecular motor, ξ_f, the friction coefficient between the filament and the surrounding solution and $\tilde{v}_f$, the speed of the filament in this type of assay. The first equation represents the force balance on the filament and the second equation is the force balance on the filament and motor complex. We use here a simplified expression for the motor force estimated in Eq. SE 7, i.e. (*42*),

$$f_{mot} = f_s \left(1 - \frac{v_m - \tilde{v}_f}{v_0}\right), \quad \text{(SE 12)}$$

where f_s is the stall force and v_0 the sliding speed at zero external force ($f_s \approx O(1)pN$ and $v_0 \approx 50 \frac{nm}{s}$ as calculated before with the more detailed model). The friction between the filament and the solution can be estimated as $\xi_f \approx 2\pi \, \eta_b \frac{l}{\log l/b_f} \approx O(10^{-8}) Pa.s.m$, where we take the bulk viscosity of water $\eta_b = O(10^{-3}) Pa.s$ and as characteristic lengthscale, the size of the filament $l = O(10^{-5})m$. Note however that the effective bulk viscosity can be significantly larger since the filament slides close to a surface. The friction between the motor complex and the lipid $\xi_m \approx 4\pi \frac{\eta_m}{\log\left(\frac{l_0}{L}\right)} \approx O(10^{-9})$Pa.s.m (*43*), where L is the size of the membrane and l_0 the size of the motor (we estimate the membrane viscosity as $\eta_m \approx O(10^{-10}) Pa.s.m$ (*44*) and $\log(L/l_0) \approx O(1)$). Solving equations SE 10 and SE 11 gives the following values for the velocity of the filament, $\tilde{v}_f$, relative to the velocity at zero external force on a solid substrate, v_0,

$$\frac{\tilde{v}_f}{v_0} = -\frac{n\xi_m}{\xi_f + n\xi_m + v_0 \xi_f \xi_m / f_s}, \quad \text{(SE 13)}$$

and for the velocity of the motor, v_m,

$$\frac{v_m}{v_0} = \frac{\xi_f}{\xi_f + n\xi_m + v_0 \xi_f \xi_m / f_s}, \quad \text{(SE 14)}$$

For realistic values of the friction coefficient of water and typical force values we obtain a filament speed which is very close to the filament speed on a solid substrate $\tilde{v}_f / v_f \approx 1$, indicating that, since the in-plane membrane friction of the motor is larger than the filament friction with the fluid, the motors are effectively immobile. However, upon increasing the viscous friction between the filament and the bulk by one/two orders of magnitude, potentially due to inter-filament friction (at high filament density) or interactions with the methyl cellulose, the sliding speed of the filament diminishes significantly (See Fig. S4B). Also decreasing the density of motors along the filament impacts the sliding speed since the effective friction between membrane and motor is proportional to the density of motors.

bioRxiv preprint doi: https://doi.org/10.1101/375923; this version posted July 24, 2018. The copyright holder for this preprint (which was not certified by peer review) is the author/funder. All rights reserved. No reuse allowed without permission.

Legends - Supplementary figures

Table S1: Sliding velocities v_f of stabilized and polymerizing actin filaments on Myo1b or Myosin II in the different used conditions.

Table S2: Rate constants of G-actin monomer association and dissociation in the absence and presence of Myo1b or Myosin II in the different used conditions.

Figure S1: Analysis of the experimental data and calibration of the Myo1b density. **A)** Left: Time-lapse images obtained by TIRF microscopy of a stabilized filament (top) (movie S1) and a polymerizing filament in the presence of 1.2 µM G-actin (bottom) (movie S2) sliding along glass-anchored Myo1b. White dots indicate the filament barbed end. The white dashed represents the trajectory of the stabilized filament, and ΔX the total displacement of the filament over the period considered. L_0 and ΔL are the initial length of the polymerizing filament and its elongation, respectively. Middle: corresponding kymographs. The sliding ΔX and the elongation ΔL correspond to the white arrows. Right: Time variation of ΔX and ΔL. The sliding v_f and elongation v_p velocities are deduced from the slopes of the graphs. Actin fluorescence intensity is represented according to the "Fire" LUT of Image J. Scale bar, 5µm. 1 image/20 sec. **B)** Myo1b density on the solid substrate or the supported bilayer deduced from (a) the measurement of the fluorescence intensity of a reference lipid Atto488DOPE at known density in a SLB (supported lipid bilayer), and the comparison of (b) the fluorescence of Myo1b dye Alexa 488 and (c) Atto488DOPE in bulk at known concentrations (see Materials and Methods). The calibration constant A is deduced from the slope of a).

Figure S2: Impact of Myo1b on F-actin minus end and impact of Myo1b at low density, inactivated, or in solution on the sliding and actin depolymerization at the barbed end. **A)** Representative kymographs of polymerizing actin filaments, in presence of 0.6 µM G-actin, 2 mM ATP with anchored Myo1b at ≈ 8000 μm^{-2} (see movie S7). The elongation ΔL_m of the filaments at the minus end (between the 2 dashed white lines) is indicated. Scale bar, 5 µm. 1 image/10 sec. **B)** Representative kymographs of phalloidin stabilized filaments (top) or polymerizing actin filaments (bottom), in presence of 0.6 µM G-actin, 2 mM ATP, with Myo1b in solution (red), Myo1b without motor activity (brown), with anchored Myo1b at low density (≈500 motor/μm^2) (purple). (See movies S5 and S8). Scale bar, 5µm. 1image/10 sec. **C)** Comparison of the distribution of the velocities v_f of stabilized (top) and polymerizing F-actin (bottom) sliding on immobilized high density Myo1b (dark blue) and low density Myo1b (purple). Velocity distributions and average velocities are indicated. **D)** ΔL versus time for the single filaments shown in (B). **E)** v_p as a function of G-actin concentration C_m for the different conditions. The fit to the data is the same as in Fig. 2D. Error bars represent s.e.m. (n > 25). Inset: k_{off} for the different conditions. **F)** Representative kymographs of polymerizing actin filaments, in presence of 0.3 µM G-actin, 2 mM ATP, without Myo1b, with anchored Myo1b at ≈8000 motor/μm^2. (See movie S10). Scale bar, 5µm. 1 image/10 sec. **G)** ΔL versus time for the single filaments shown in (F). **H)** v_p as a function of filament length L for single polymerizing filaments sliding along glass-anchored Myo1b in the presence of 0.6 µM G-actin and 2 mM ATP (n = 90, v_p measured during 30 sec).

Figure S3: Theoretical model for filament sliding. **A)** Two-state cross-bridge model consisting of two populations of motors: a fraction ξ of "active" motors (colored) bind ATP and perform a power-stroke and a fraction 1−ξ of "passive" motors (in grey). **B)** Instantaneous average force acting on the filament for the active (solid line) and passive motors (dashed

bioRxiv preprint doi: https://doi.org/10.1101/375923; this version posted July 24, 2018. The copyright holder for this preprint (which was not certified by peer review) is the author/funder. All rights reserved. No reuse allowed without permission.

line) (Eq. SI8). Note that a positive force implies a propulsive force while a negative force corresponds to a friction-like force. **C)** Theoretical force-velocity curve for a catch-bond type motor (blue) and a force-independent motor (neither catch-bond or slip-bond) with otherwise identical parameters (blue dashed). This indicates that, for otherwise identical parameters, in the absence of externally applied force ($F=0$) (*), the velocity significantly decreases for the catch-bond motor. **D)** Effect of ATP concentration on the force-velocity curve for the catch-bond motor: 2 μM (blue, corresponding to Fig. S2C) and 0.2 μM (purple). Increasing the ATP concentration increases the number of "active" motors and hence increases the sliding velocity proportionally. **E)** Prediction for the effect of ATP concentration on the sliding velocity.

Figure S4: Impact of filament sliding on depolymerization. A) Theoretical prediction for the impact of the ATP concentration, $C_{ATP}[mM]$, on the depolymerization rate, relative to its value at vanishing force, k_d/k_d^0, for various values of the characteristic force scale F^*. Increasing the ATP concentration increases the force of the filament and hence increases the depolymerization rate. **B)** Velocity of the filament, relative to its velocity on a solid substrate (Eq. SI 13) for various values of motor density n. Increasing the bulk viscosity, relative to the membrane viscosity, induces motion of the motors in the bilayer, hence decreasing the effective velocity of the filament. Increasing the density of molecular motors on the surface increases the effective membrane friction and hence increases the sliding speed.

Figure S5: Myo1b bound to giant liposomes produces membrane invagination in presence of stabilized actin filaments.
Confocal microscopy image of Myo1b bound to a PI(4,5)P_2-containing GUV and recruitment of stabilized actin filaments. Labeling corresponds to (a) 0.3% Texas Red DHPE (mol/mol) and (b) stabilized actin filaments with Alexa Fluor 647 phalloidin. Scale bars, 5 μm.

Legends – Movies

Movie S1: Stabilized actin filament sliding along glass-anchored Myo1b.
TIRFM visualization of the sliding of stabilized single filament labeled with phalloidin-Alexa547 along Myosin 1b (8000 μm^{-2}) at 2 mM ATP. Movie S1 is related to Fig. S1A (top panel). Scale bar 5 μm. Time in s.

Movie S2: Polymerizing actin filament sliding along glass-anchored Myo1b.
TIRFM visualization of the sliding of polymerizing single filament with 1.2 μM actin in bulk (10 % Alexa594 labeled), along Myosin 1b (8000 μm^{-2}) at 2 mM ATP. Movie S2 is related to Fig. S1A (bottom panel). Scale bar 5 μm. Time in s.

Movie S3: Effect of the ATP concentration on stabilized actin filaments sliding along glass-anchored Myo1b.
TIRFM visualization of the sliding of stabilized single filaments with phalloidin-Alexa547 along Myosin 1b (8000 μm^{-2}) at 2 mM (a) and 0.2 mM (b) ATP. Movie S3 is related to Fig. 2A (top panel). Scale bar 5 μm. Time in s.

bioRxiv preprint doi: https://doi.org/10.1101/375923; this version posted July 24, 2018. The copyright holder for this preprint (which was not certified by peer review) is the author/funder. All rights reserved. No reuse allowed without permission.

Movie S4: Effect of ATP concentration on polymerizing actin filaments sliding along glass-anchored Myo1b.
TIRFM visualization of the sliding of polymerizing single filaments, with 0.6 µM actin (10 % Alexa594 labeled), along Myosin 1b (8000 μm^{-2}) at 2 mM (a) and 0.2 mM (b) ATP. Movie S4 is related to Fig. 2A (bottom panel). Scale bar 5 µm. Time in s.

Movie S5: Stabilized and polymerizing actin filaments sliding along Myo1b at low density.
TIRFM visualization of the sliding of stabilized single filaments labeled with phalloidin-Alexa547 (a, left) and polymerizing actin filaments (b, right), with 0.6 µM actin (10 % Alexa594 labeled), along Myo1b at low density (400 μm^{-2}) at 2 mM ATP. Movie S5 is related to Fig. S2B. Scale bar 5 µm. Time in s.

Movie S6: Stabilized and polymerizing actin filaments in absence of Myo1b.
TIRFM visualization of stabilized single filaments with phalloidin-Alexa547 (a, left) and polymerizing actin filament (b, right), with 0.6 µM actin (10 % Alexa594 labeled), without Myo1b at 2 mM ATP. Movie S6 is related to Fig. 2A. Scale bar 5 µm. Time in s.
Movie S7: No effect at minus-end on polymerizing actin filaments sliding along glass-anchored Myo1b.
TIRFM visualization of polymerizing actin filaments (a and b), with 0.6 µM actin (10 % Alexa594 labeled), along Myosin 1b (8000 μm^{-2}) at 2 mM ATP. Movie S7 is related to Fig. S2A. Scale bar 5 µm. Time in s.

Movie S8: Stabilized and polymerizing actin filaments with Myo1b in bulk and inactivated.
TIRFM visualization of stabilized single filament with phalloidin-Alexa547 (a and c, left) and polymerizing actin filament (b and d, right), with 0.6 µM actin (10 % Alexa594 labeled), with 300 nM Myo1b in the bulk (a and b, top) and inactivated (c and d, bottom) at 2 mM ATP. Movie S8 is related to Fig. S2B. Scale bar 5 µm. Time in s.

Movie S9: Stabilized and polymerizing actin filaments sliding along glass-anchored Myosin II.
TIRFM visualization of the sliding of stabilized single filament with phalloidin-Alexa547 (a, left) and polymerizing actin filament (b, right), with 0.6 µM actin (10 % Alexa594 labeled), along Myosin II at 2 mM ATP. Movie S9 is related to Fig. 2A. Scale bar 5 µm. Time in s.

Movie S10: Polymerizing actin filament sliding along glass-anchored Myo1b, above the critical actin concentration in the absence of Myo1b
TIRFM visualization of polymerizing single filament with 0.3 µM actin in bulk (10 % Alexa594 labeled), without Myosin 1b (a, left), along Myosin 1b (b, right), at 2 mM ATP. Movie S10 is related to Fig. S2F. Scale bar 5 µm. Time in s.

Movie S11: Stabilized and polymerizing actin filaments sliding along Myo1b bound to SLBs.
TIRFM visualization of the sliding of stabilized single filament with phalloidin-Alexa547 (a, left) and polymerizing actin filament (b, right), with 0.6 µM actin (10 % Alexa594 labeled), along Myo1b bound to SLBs (≈ 8500 μm^{-2}) at 2 mM ATP. Movie S11 is related to Fig. 3B. Scale bar 5 µm. Time in s.

bioRxiv preprint doi: https://doi.org/10.1101/375923; this version posted July 24, 2018. The copyright holder for this preprint (which was not certified by peer review) is the author/funder. All rights reserved. No reuse allowed without permission.

Table S1

	Myosin	[ATP] (mM)	Density (molecules/μm^2)	Condition	Velocity (nm/s)
On glass	Myosin 1b	2	8393 ± 430	No polymerization	56.4 ± 15.4
		2	8444 ± 873	Polymerization	53.9 ± 5.5
		0.2	8776 ± 1293	No polymerization	24.7 ± 4.2
		0.2	8876 ± 459	Polymerization	27.2 ± 1.9
		2	447 ± 20	No polymerization	33.3 ± 3.1
		2	533 ± 84	Polymerization	35.6 ± 6.2
	Myosin II	2	Not reported	No polymerization	257 ± 76
		2	Not reported	Polymerization	279 ± 68
On SLB	Myosin 1b	2	8770 ± 170	No polymerization	37.6 ± 7.3
		2	8657 ± 1251	Polymerization	39.3 ± 8.2

Table S2

	Myosin	[ATP] (mM)	Density (molecules/μm^2)	k_{on} (su.μM^{-1}.s^{-1})	k_{off} (su.s^{-1})	Critical concentration C_{c+} (μM)
In solution	No Myosin	0.2		10.3 ± 0.8	1.1 ± 0.4	0.10 ± 0.05
	No Myosin	2		10.9 ± 0.6	1.4 ± 0.4	0.13 ± 0.06
	Myosin 1b	2	Not reported	11.4 ± 1.1	1.8 ± 0.5	0.16 ± 0.04
On glass	Myosin 1b	2	8444 ± 873	10.3 ± 0.5	3.2 ± 0.4	0.31 ± 0.05
		0.2	8876 ± 459	10.7 ± 0.9	2.1 ± 0.5	0.20 ± 0.04
		2	533 ± 84	10.0 ± 1.2	2.6 ± 0.6	0.26 ± 0.08
	No motor	2	7767 ± 423	10.9 ± 0.8	1.6 ± 0.5	0.15 ± 0.05
	Myosin II	2	Not reported	10.0 ± 0.8	1.0 ± 0.5	0.10 ± 0.05
On SLB	Myosin 1b	2	8657 ± 1251	9.9 ± 0.8	2.5 ± 0.5	0.26 ± 0.05

bioRxiv preprint doi: https://doi.org/10.1101/375923; this version posted July 24, 2018. The copyright holder for this preprint (which was not certified by peer review) is the author/funder. All rights reserved. No reuse allowed without permission.

Figure S1

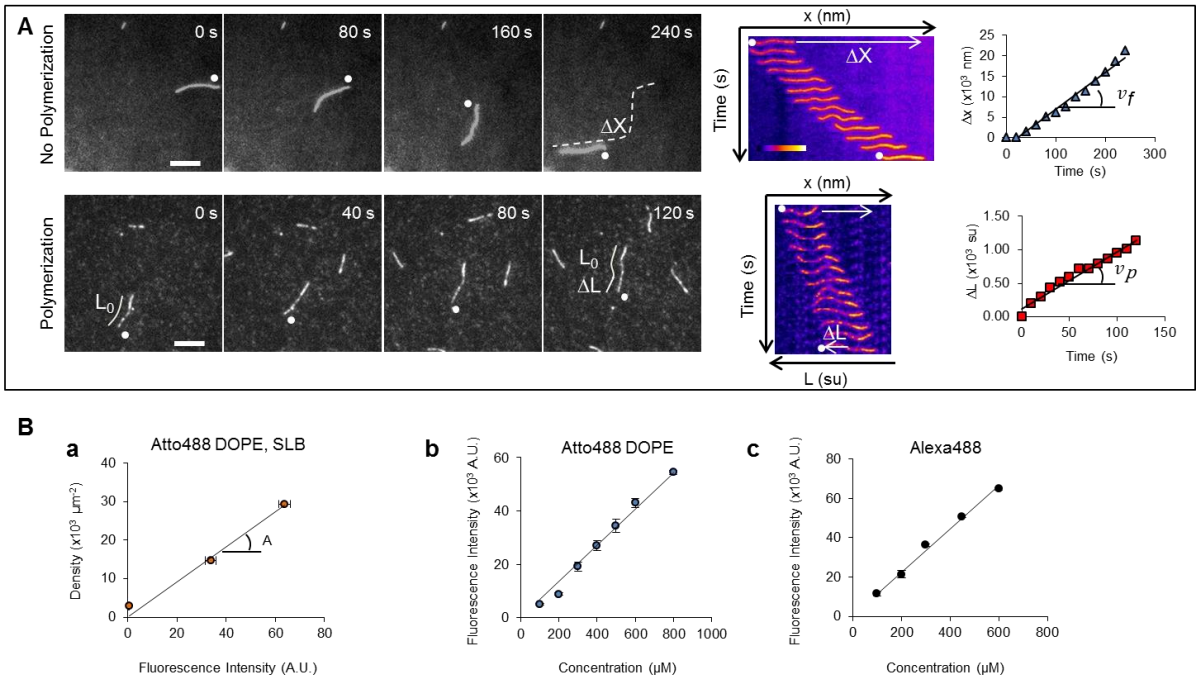

bioRxiv preprint doi: https://doi.org/10.1101/375923; this version posted July 24, 2018. The copyright holder for this preprint (which was not certified by peer review) is the author/funder. All rights reserved. No reuse allowed without permission.

Figure S2

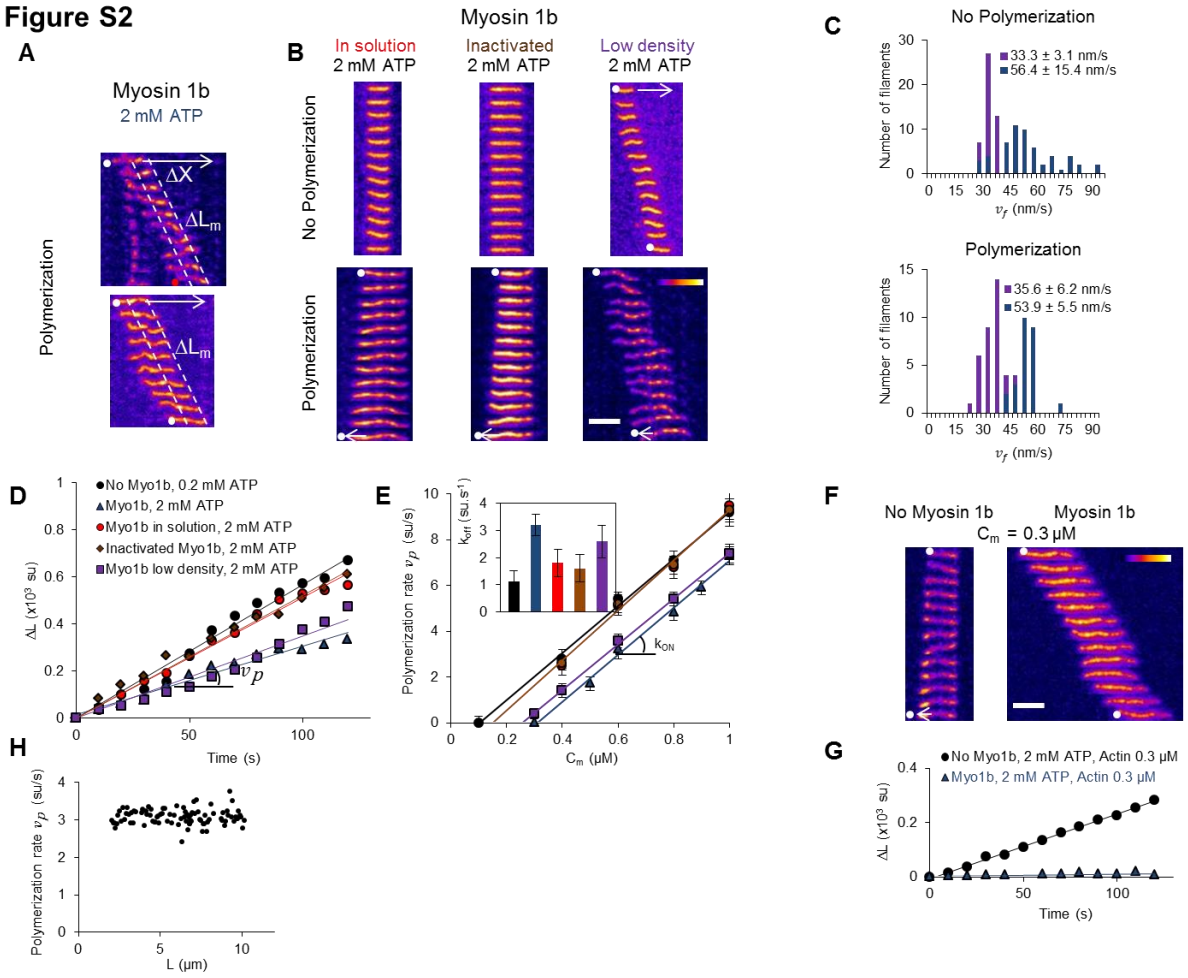

bioRxiv preprint doi: https://doi.org/10.1101/375923; this version posted July 24, 2018. The copyright holder for this preprint (which was not certified by peer review) is the author/funder. All rights reserved. No reuse allowed without permission.

Figure S3

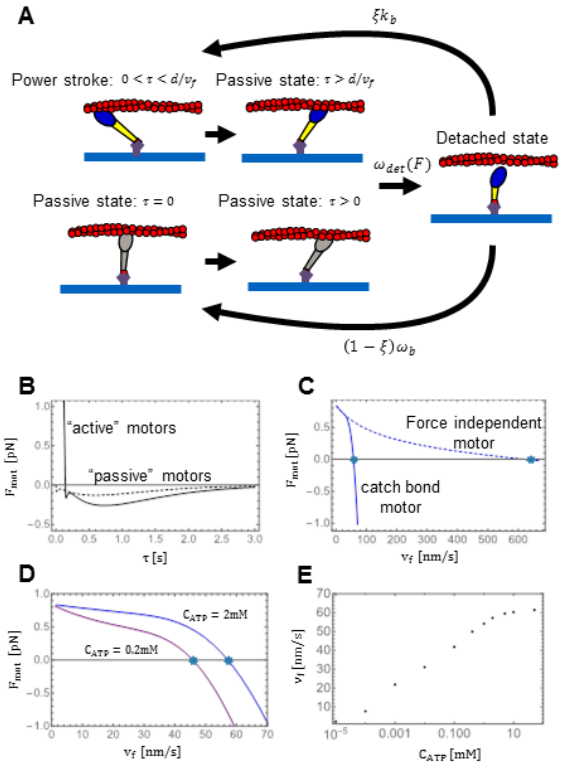

bioRxiv preprint doi: https://doi.org/10.1101/375923; this version posted July 24, 2018. The copyright holder for this preprint (which was not certified by peer review) is the author/funder. All rights reserved. No reuse allowed without permission.

Figure S4

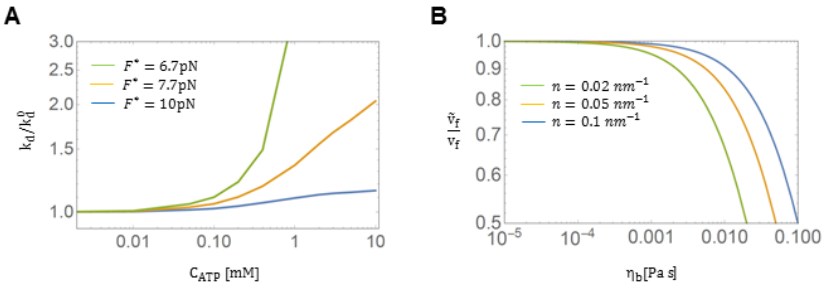

bioRxiv preprint doi: https://doi.org/10.1101/375923; this version posted July 24, 2018. The copyright holder for this preprint (which was not certified by peer review) is the author/funder. All rights reserved. No reuse allowed without permission.

Figure S5